Journal of Alloys and Compounds 500 (2010) 153–160

Contents lists available at ScienceDirect

Journal of Alloys and Compounds

journal homepage: www.elsevier.com/locate/jallcom

o'-$Al_{13}Co_4$, a new quasicrystal approximant

F. Fleischer*, T. Weber, D.Y. Jung, W. Steurer

Laboratory of Crystallography, ETH Zurich, 8093 Zurich, Switzerland

ARTICLE INFO

Article history:
Received 5 March 2010
Received in revised form 18 March 2010
Accepted 19 March 2010
Available online 30 March 2010

Keywords:
Intermetallics
Crystal structure
Order–disorder effects
X-ray diffraction
Computer simulations

ABSTRACT

The crystal structure of o'-$Al_{13}Co_4$, a new $Al_{13}TM_4$ (TM = transition metal) modification was determined by single-crystal X-ray diffraction. The phase, with Pearson symbol $oP204-x$ ($x = 6$), crystallizes in the orthorhombic space group *Pnma* (No. 62) with lattice parameters $a = 28.890(4)$ Å, $b = 8.138(2)$ Å and $c = 12.346(1)$ Å. The structure, which can be seen as a stacking of four flat and puckered atomic layers along the pseudo-tenfold b axis, is closely related to o-$Al_{13}Co_4$ and m-$Al_{13}Co_4$. First-principles total-energy calculations indicate that all these related $Al_{13}Co_4$ modifications, some of them stabilized by vacancies, seem to be slightly unstable at low temperatures.

1. Introduction

The system Al–Co has been intensively investigated in the context of quasicrystals and complex intermetallic compounds (for a review see [1]). Several complex stable and metastable phases with compositions between Al_5Co_2 and Al_9Co_2 have been found between room temperature and approximately 1150 °C [2–5]. The structures can be seen as approximants to decagonal quasicrystals.

All structures with compositions between Al_5Co_2 and Al_9Co_2 are members of the $Al_{13}TM_4$ (TM = transition metal) structure family. The centered monoclinic structure m-$Al_{13}Co_4$ with composition $Al_{75.2}Co_{24.8}$ ($mC102-x$, $x = 5$, $a = 15.183(2)$ Å, $b = 8.122(1)$ Å, $c = 12.340(2)$ Å, $\beta = 107.54(1)°$) [6] is essentially isostructural to $Al_{13}Fe_4$[7,8], $Al_{13}Ru_4$[9] and $Ni_3Zn_6Ga_4$ (Zn and Ga replace Al positions and Ni sits on Fe sites) [10].

The crystal structure of the closely related orthorhombic phase o-$Al_{13}Co_4$ ($oP102$, $a = 8.158(1)$ Å, $b = 12.342(1)$ Å, $c = 14.452(2)$ Å, $Pmn2_1$) was reported without any partially occupied positions [11]. Comprehensive studies of anisotropic magnetic and transport properties of o-$Al_{13}Co_4$ were performed by [12].

τ^2-$Al_{13}Co_4$ is the largest known approximant of a decagonal quasicrystal; due to the difficulty of growing single crystals of this incongruent melting phase, no quantitative single-crystal X-ray structure analysis has been published so far. Compared to m-$Al_{13}Co_4$, this C-centered monoclinic structure has $\sim\tau^2$ times (τ: golden mean, $\tau = (1+\sqrt{5})/2 \approx 1.61803\ldots$) larger lattice parameters a and c ($a = 39.84$ Å, $b = 8.148$ Å, $c = 32.23$ Å, $\beta = 107.97°$) and was first identified by high-resolution electron microscopy (HRTEM) [13]. Structure models of the τ^2 phase were derived by HRTEM [14] and high-angle annular dark-field scanning transmission electron microscopy (HAADF-STEM) [15]. The fundamental atomic clusters with 2 nm diameter were found to be similar to those identified in decagonal Al–Ni–Fe, Al–Cu–Co and Al–Co–Ni.

Furthermore, a stable high-temperature phase ht-Al_3Co with composition close to $Al_{13}Co_4$ was found and its stability range extensively discussed [3,4,16]. It is isostructural to $Al_{13}Os_4$ ($C2/m$, $a = 16.989(4)$ Å, $b = 4.098(1)$ Å, $c = 7.478(2)$ Å, $\beta = 115.812(5)°$) [17].

In the following we discuss the structure and stability of a new orthorhombic phase, o'-$Al_{13}Co_4$, in the Al–Co system and show its close relationships to o-$Al_{13}Co_4$ and m-$Al_{13}Co_4$. First-principles total-energy calculations on several models of all these phases show their stability and how it is increased by a proper distribution of vacancies.

2. Experimental

2.1. Sample preparation

An ingot of about 8 g with the nominal composition of the τ^2 phase ($Al_{74.6}Co_{25.4}$) was prepared from the elements Al and Co (shots, 5N grade) using a levitation induction furnace operated under argon atmosphere. The pre-alloy was quenched in a water-cooled copper-cylinder with 8 mm diameter. The phase composition of the as-cast ingot was determined by powder X-ray diffraction and indicates a major content of the τ^2 phase and a minor content of m-$Al_{13}Co_4$. The as-cast rod was cut into pieces, put into corundum crucibles and annealed at 1050 °C for 82 d in evacuated and sealed quartz glass ampoules. The structure was determined on crystals from samples cooled down to room temperature with a cooling rate of 300 K/h between 1050 °C and 500 °C and of about 100 K/h below. Samples that were further annealed at 1140 °C for 6 d, 1100 °C for 10 d and 1000 °C for 10 d and water quenched afterwards show the same single-crystal X-ray diffraction patterns as the slowly cooled

* Corresponding author. Tel.: +41 44 6323776; fax: +41 44 6321133.
E-mail addresses: frank.fleischer@mat.ethz.ch (F. Fleischer), steurer@mat.ethz.ch (W. Steurer).

0925-8388/$ – see front matter © 2010 Elsevier B.V. All rights reserved.
doi:10.1016/j.jallcom.2010.03.188

Table 1
Crystallographic information, data collection and structure refinement data.

Crystal data	
Chemical formula	$Al_{148.15}Co_{50}$
M_r	6943.59
D_x/D_m (Mg m^{-3})	3.972/4.00(1)
Cell settings, space group	Orthorhombic, *Pnma*
Temperature (K)	293
a (Å)	28.890(4)
b (Å)	8.138(2)
c (Å)	12.346(1)
V (Å^3)	2902.63(6)
Z	1
Radiation type	Synchrotron
Wavelength (Å)	0.70850/0.69393
μ (mm^{-1})	8.076
Crystal form, size (mm)	Irregular, 0.06 × 0.04 × 0.04
Data collection	
Diffractometer	Pilatus 6M pixel detector/mar345 image plate detector
Data collection method	φ-scan
Absorption correction	Multi-scan
No. of measured, independent and observed reflections	118534, 4164, 4001
Criterion for observed reflections	$I > 2\sigma(I)$
R_{int}	0.0481
θ_{max} (°)	30.35
Refinement	
Refinement method	Full-matrix least-squares on F^2
$R[F^2 > 2\sigma(F^2)]$, $wR(F^2)$, S	0.0307, 0.0864, 1.066
No. of reflections	4164
No. of parameters	277
$(\Delta/\sigma)_{max}$	0.001
$\Delta\sigma_{max}$, $\Delta\sigma_{min}$ (eÅ^{-3})	2.598, −1.342

sample. In addition, single crystals smaller than 0.1 mm × 0.1 mm × 0.1 mm size were annealed for 10 min at 1100 °C using an infrared microfurnace equipped with an optical microscope. Independent of the annealing temperature and the cooling protocol, always o'-$Al_{13}Co_4$ was observed by single-crystal X-ray diffraction.

The chemical composition of a 2 mm × 2 mm × 2 mm sized sample, taken from the neighborhood of the investigated single crystals, was determined to $Al_{74.5(3)}Co_{25.5(3)}$ based on 23 point measurements with a JEOL JXA-8200 WD/ED combined microprobe. Back-scattered electron images and powder diffraction investigations identified the alloy as single phase. The density of the sample was measured to 4.00(1) Mg m^{-3}. For comparison, the observed density of m-$Al_{13}Co_4$ (with nominal composition $Al_{73.6}Co_{26.3}$) was reported to be 3.81(5) Mg m^{-3} [6] and the density of o-$Al_{13}Co_4$ was calculated based on its crystal structure to 4.02 Mg m^{-3} [ICSD (inorganic crystal structure database) code: 104638].

2.2. Data collection and processing

A first single-crystal X-ray diffraction data set was collected at the Swiss-Norwegian beam line (SNBL) at the European Synchrotron Radiation Facility (ESRF) in Grenoble, France, using a mar345 image plate detector system (wavelength λ = 0.69393 Å, 111 frames, oscillation angle per frame $\Delta\phi$ = 1.0°, exposure time t_{exp} = 5 s/frame) as well as at the X06SA beam line at the Swiss Light Source (SLS) in Villigen, Switzerland, using a Dectris PILATUS6M pixel detector (λ = 0.70850 Å, 10,000 frames, $\Delta\phi$ = 0.1°, t_{exp} = 0.1 s/frame). For further details see Table 1. The energy threshold of the PILATUS detector was set to suppress fluorescence scattering from Co. Both data sets were collected on the same crystal and processed with the XDS program package [18]. The PILATUS data were collected in addition to the previously measured image plate data because of the exceptional power of this detector for the measurement of weak Bragg and diffuse scattering data [19,20]. Due to the large dynamic range of the diffraction intensities, very strong reflections in the PILATUS data set were saturated. To have a complete diffraction data set the resulting reflection files from both experiments were merged with the program XDS.

3. Results and discussion

3.1. Structure determination and refinement

Reciprocal space reconstructions based on the PILATUS data are shown in Fig. 1. The diffraction pattern, with Laue symmetry *mmm*, shows the systematic reflection conditions $h\,0\,0 : h = 2n$, $0\,k\,0 : k = 2n$, $0\,0\,l : l = 2n$, $h\,k\,0 : h = 2n$ and $0\,k\,l : k + l = 2n$ and, in addition, the pseudo-reflection condition $h\,k\,0 : h + 2k = 4n$. All reflection conditions as well as the *mmm* Laue symmetry are partly violated by very weak reflections observable only with the PILATUS detector. Most of these weak reflections do not obey Friedel's law and may originate from *Umweganregung*. Reflections breaking the pseudo-reflection condition $h\,k\,0 : h + 2k = 4n$ are stronger and in a better agreement with Friedel's law. Reciprocal space layers perpendicular to **b*** show the pseudo-tenfold symmetry (Fig. 1b) typical for approximants of decagonal quasicrystals.

The structure was solved using SUPERFLIP [21], a program for performing iterative phase-retrieval methods like charge flipping [22,23] and low-density elimination [24]. The space group *Pnma* was derived using a symmetry-determination algorithm [25], which analyses the electron density for the presence of symmetry operators compatible with the metric of the unit cell. The high quality of the electron density map allowed a correct identification of all fully occupied Al and Co sites. The least-squares refinement was done with SHELXL97 [26]. After initial refinement steps, strong residuals were observed within a zigzag line of partially occupied Al atoms. The R-values could be drastically decreased from R = 0.069 to R = 0.031 by modeling the partially occupied atoms in the zigzag line and at some Al positions next to this region as complex split positions (Fig. 2b). The split atoms were constrained to have the same isotropic atomic displacement parameters (ADPs). The outer Al atoms (Al22 and Al23) are split in two positions and have an approximate site occupation factor (SOF) of 0.5 for each atom. The four symmetry-independent Al positions (Al24–Al27) show a more complex situation. They were refined to a total occupation of ∼3.0 and finally yield 11 split positions. Al24 and Al25 split into two positions and Al26 and Al27 are each distributed over three split sites. One residual peak in the difference map was modeled with an additional partially occupied Al (Al28). In summary, a complex splitting of six Al atoms can describe the zigzag line and partial occupation leads to a total of about one vacancy per zigzag line. No split positions are reported for o-$Al_{13}Co_4$ [11] and m-$Al_{13}Co_4$, but partial occupations were observed for Al atoms in the monoclinic phase [6,27], which have similar structural environments as the partially occupied Al atoms of the o'-$Al_{13}Co_4$ structure.

After the initial refinements one of the Al sites showed negative ADPs. Therefore, this site was refined as a partially occupied Co atom (Co11, SOF = 0.52(1)). Atoms having a similar structural environment in the compounds m-$Al_{13}Co_4$ and o-$Al_{13}Co_4$ were reported as fully occupied Al sites. We, however, prefer an interpretation as a partially occupied Co atom in o'-$Al_{13}Co_4$, not only because it yields a slightly lower R-value (R decreases from 0.033 to 0.031), but also because the ADPs become positive defined and the refined composition of $Al_{74.77}Co_{25.23}$ fits the experimental results of $Al_{74.5(3)}Co_{25.5(3)}$ more accurately. Refinements in subgroups of *Pnma*, including the corresponding twin models, if applicable, did not improve the results. The final structure is shown in Fig. 2 and all data collection and refinement parameters are listed in Tables 1 and 2.

Fig. 3 shows the I_{obs} *vs.* I_{calc} scatter plot, which confirms the high quality of the refinement. Apart from a few outliers, the calculated intensities are very close to the experimental values. The weakest reflections are biased towards $I_{obs} > I_{calc}$, what may be due to systematic errors in the integration procedure, a consequence of moderate *Umweganregung* or to minor shortcomings of the model. Most prominent features in the difference Fourier maps are found close to the areas of the disordered zigzag line, *i.e.* major disagreements of the model are due to the not perfectly described complex disorder in this region.

We checked the structure model obtained by our least-squares refinements by maximum entropy (MEM) calculations using the program BayMEM [28]. The results are in a good agreement with those of the refinements and clearly indicate the presence of the

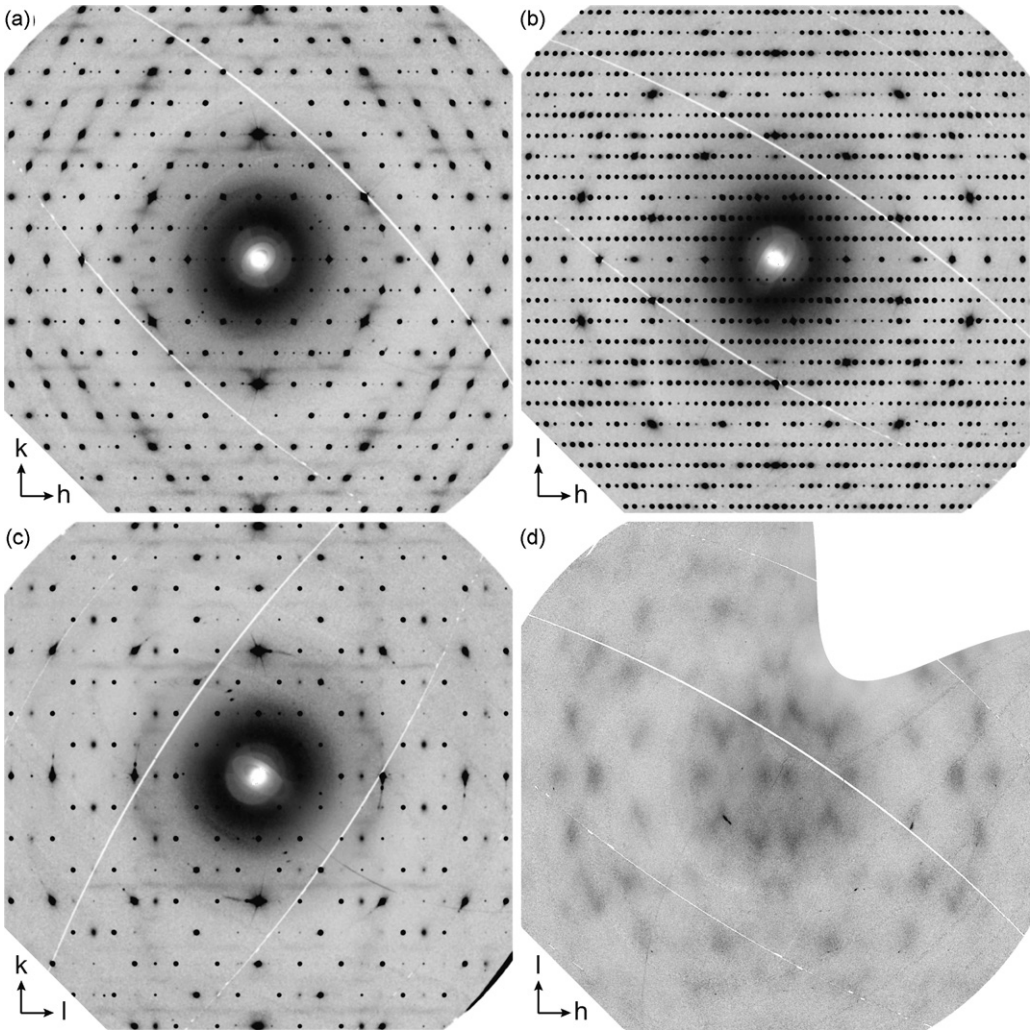

Fig. 1. Reconstructions of the $h\,k\,0$ (a), $h\,0\,l$ (b), $0\,k\,l$ (c) and $h\,3.5\,l$ (d) reciprocal space layers from the PILATUS detector based experiment at the SLS. The sections cover a region of ± 1 Å^{-1} along both directions. Note that the contrast in the images is set such that the weakest features can be seen. Black pixels correspond to an intensity of > 4 counts/pixel in the raw data. The reconstructed data were convoluted with isotropic two-dimensional Gaussians with FWHM = 0.006 Å^{-1} (the experimental width is about 0.003 Å^{-1}) to make the weak reflections better visible. The white arcs in the images are caused by the blind area of the detector.

zigzag sequence of partially occupied Al split positions in the flat layers (Fig. 4).

3.2. Structural building principles

The structure can be described as a four layer stacking along the *b* direction with ∼8 Å periodicity (Fig. 2). The two atomic layers at $y = 0$ and $y = 0.5$ are puckered while the others at $y = 0.25$ and $y = 0.75$ are flat. The most prominent structure motifs are pentagonal bipyramids (PBP) with Co atoms at the vertices (Fig. 5). The PBP appear as large pentagons in the flat layers (Fig. 2b). The apical Co atoms of the PBPs, pentagonally surrounded by Al atoms, form the vertices of a hexagon tiling in the puckered layers (Fig. 2a). The same kind of building units was already observed for several approximants such as *m*-$Al_{13}TM_4$ (TM = Fe, Co, Ru) [7,8,29,6,27,9], *o*-$Al_{13}Co_4$[11], *m*-$Al_{13}(Co,Ni)_4$[30] or Al_9Co_2Ni [31].

Along *b* and *c*, the lattice parameters of *o*′-$Al_{13}Co_4$ are similar to *o*-$Al_{13}Co_4$ but approximately doubled along *a*.[1] The structures of *o*′-$Al_{13}Co_4$, *o*-$Al_{13}Co_4$ and *m*-$Al_{13}Co_4$ are closely related to each other, they can be described by the same unit tiles (pentagons, hexagons, rhombs) in different arrangements. However, locally the structures are quite similar despite their description by different tilings as illustrated in Fig. 6. To show the similarities in detail, the rhomb/pentagon and the hexagon tiling of *o*′-$Al_{13}Co_4$ is overlaid all three structures in order to identify the main differences (Fig. 7). The shaded areas mark the regions in the structures of *o*- and *m*-$Al_{13}Co_4$ where the local agreement with the structure of *o*′-$Al_{13}Co_4$ is best. It is obvious that the structures are closely related.

The non-crystallographic pseudo-reflection condition $h\,k\,0 : h + 2k = 4n$ observed for *o*′-$Al_{13}Co_4$ can be explained by the local structural similarity of *o*′- and *m*-$Al_{13}Co_4$. In its projection along *c*, the structure of *o*′-$Al_{13}Co_4$ is similar to the corresponding projection of *m*-$Al_{13}Co_4$. Consequently, the $h\,k\,0$ reciprocal space sections are expected to be similar in both cases and the reflection condition $h\,k\,0 : h + k = 2n$ of *C*-centered *m*-$Al_{13}Co_4$ applies to *o*′-$Al_{13}Co_4$ as well: from the transformation $\mathbf{a}^*_m \approx 2\mathbf{a}^*_o$ follows $h\,k\,0 : 1/2h + k = 2n$ *i.e.* $h + 2k = 4n$ in terms of the *o*′-$Al_{13}Co_4$ lattice.

3.3. Diffuse scattering and disorder

All diffuse features observed for *o*- and *m*-$Al_{13}Co_4$ are extremely weak and could only be measured with the PILATUS6M detector,

[1] Note the different settings for *o*′-$Al_{13}Co_4$ and *o*-$Al_{13}Co_4$: $\mathbf{abc}_{o'} \leftrightarrow \boldsymbol{cab}_o$. In the following we refer to the setting *o*′-$Al_{13}Co_4$ if not stated otherwise.

Table 2
Fractional atomic coordinates and isotropic or equivalent isotropic and atomic displacement parameters (Å^2).

Label	*x*	*y*	*z*	Occ.	Ueq, Uiso*	U11	U22	U33
Co1	0.215902(10)	0.02816(5)	0.43603(2)	1.0	0.01260(9)	0.00682(14)	0.02280(17)	0.00819(14)
Co2	0.168326(13)	0.25	0.74196(3)	1.0	0.00736(9)	0.00632(17)	0.00707(17)	0.00868(18)
Co3	0.081933(13)	0.25	0.44519(3)	1.0	0.00726(9)	0.00622(16)	0.00692(17)	0.00864(17)
Co4	0.425735(12)	0.25	0.93078(3)	1.0	0.00721(9)	0.00648(16)	0.00628(17)	0.00886(17)
Co5	0.170825(11)	0.25	0.13845(3)	1.0	0.00686(9)	0.00497(15)	0.00654(16)	0.00907(18)
Co6	0.324870(13)	0.25	0.25674(3)	1.0	0.00778(10)	0.00622(17)	0.00695(18)	0.0102(2)
Co7	0.034247(10)	0.02849(5)	0.74856(2)	1.0	0.01070(9)	0.00664(14)	0.01749(16)	0.00796(14)
Co8	0.424670(12)	0.25	0.57386(3)	1.0	0.00625(9)	0.00530(16)	0.00716(16)	0.00631(16)
Co9	0.078902(12)	0.25	0.04830(3)	1.0	0.00701(9)	0.00484(16)	0.00691(16)	0.00928(17)
Co10	0.324737(11)	0.25	0.61367(3)	1.0	0.00606(9)	0.00574(15)	0.00674(16)	0.00570(16)
Co11	0.37421(2)	0.25	0.09263(6)	0.525(2)	0.0117(2)	0.0154(4)	0.0082(4)	0.0117(4)
Al1	0.21705(2)	0.03293(9)	0.05021(5)	1.0	0.00893(13)	0.0074(3)	0.0120(3)	0.0074(2)
Al2	0.03291(2)	0.03236(8)	0.13687(5)	1.0	0.00896(12)	0.0080(2)	0.0112(3)	0.0077(2)
Al3	0.37942(2)	0.01890(8)	0.26232(5)	1.0	0.01145(13)	0.0082(2)	0.0120(3)	0.0141(3)
Al4	0.38595(3)	0.25	0.75524(6)	1.0	0.00970(16)	0.0109(4)	0.0113(4)	0.0069(3)
Al5	0.36395(3)	0.25	0.43198(6)	1.0	0.01063(16)	0.0136(4)	0.0114(4)	0.0069(3)
Al6	0.31061(2)	0.03013(9)	0.75272(4)	1.0	0.01204(14)	0.0109(3)	0.0189(3)	0.0063(3)
Al7	0.37065(2)	0.01900(8)	0.92459(5)	1.0	0.01143(12)	0.0082(2)	0.0123(3)	0.0137(3)
Al8	0.43931(2)	0.02980(9)	0.43415(4)	1.0	0.01165(13)	0.0101(3)	0.0196(3)	0.0052(2)
Al9	0.03597(2)	0.03139(8)	0.36100(5)	1.0	0.00938(12)	0.0092(2)	0.0117(3)	0.0073(2)
Al10	0.09752(4)	0.25	0.24759(7)	1.0	0.0193(2)	0.0366(6)	0.0106(4)	0.0105(4)
Al11	0.30873(2)	0.02443(8)	0.12047(5)	1.0	0.01233(13)	0.0093(2)	0.0216(3)	0.0061(2)
Al12	0.44155(2)	0.02886(9)	0.06595(4)	1.0	0.01222(13)	0.0103(3)	0.0188(3)	0.0076(3)
Al13	0.21403(2)	0.02962(7)	0.82571(5)	1.0	0.00984(12)	0.0099(2)	0.0117(3)	0.0080(2)
Al14	0.15315(4)	0.25	0.93988(7)	1.0	0.0180(2)	0.0331(5)	0.0108(4)	0.0102(4)
Al15	0.125075(17)	0.00024(7)	0.09371(4)	1.0	0.00856(13)	0.0069(3)	0.0064(3)	0.0124(3)
Al16	0.46194(4)	0.25	0.24729(8)	1.0	0.0219(2)	0.0266(5)	0.0149(4)	0.0241(5)
Al17	0.28774(4)	0.25	0.93775(8)	1.0	0.0238(2)	0.0255(5)	0.0193(5)	0.0265(5)
Al18	0.24456(3)	0.25	0.65971(9)	1.0	0.0194(2)	0.0115(4)	0.0125(4)	0.0341(5)
Al19	0.27318(3)	0.25	0.43977(7)	1.0	0.01473(18)	0.0244(5)	0.0076(4)	0.0122(4)
Al20	0.47659(3)	0.25	0.74897(7)	1.0	0.01250(17)	0.0187(4)	0.0073(4)	0.0114(4)
Al21	0.00685(3)	0.25	0.53443(9)	1.0	0.0193(2)	0.0114(4)	0.0127(4)	0.0338(5)
Al22A	0.00132(7)	0.25	0.9842(2)	0.575(6)	0.01220(17)*			
Al22B	0.00767(10)	0.25	0.9525(3)	0.425(6)	0.01220(17)*			
Al23A	0.24830(8)	0.25	0.2043(3)	0.476(5)	0.01220(17)*			
Al23B	0.24165(8)	0.25	0.2377(2)	0.524(5)	0.01220(17)*			
Al24A	0.07651(6)	0.25	0.8440(2)	0.582(5)	0.01220(17)*			
Al24B	0.0797(3)	0.25	0.8080(13)	0.101(5)	0.01220(17)*			
Al25A	0.17247(6)	0.25	0.34477(17)	0.514(3)	0.01220(17)*			
Al25B	0.1720(2)	0.25	0.3970(6)	0.135(3)	0.01220(17)*			
Al26A	0.16254(14)	0.25	0.5359(4)	0.451(5)	0.01220(17)*			
Al26B	0.1489(4)	0.25	0.5601(8)	0.147(5)	0.01220(17)*			
Al26C	0.16822(18)	0.25	0.4904(6)	0.172(4)	0.01220(17)*			
Al27A	0.08148(17)	0.25	0.6955(5)	0.184(3)	0.01220(17)*			
Al27B	0.08821(13)	0.25	0.6496(3)	0.466(4)	0.01220(17)*			
Al27C	0.1045(4)	0.25	0.6251(6)	0.190(4)	0.01220(17)*			
Al28	0.1234(4)	0.25	0.5955(8)	0.109(3)	0.01220(17)*			

as it has no intrinsic background and allows suppression of fluorescence scattering (Fig. 1). As a consequence of the weakness of the diffuse intensities it is not possible to give a quantitative or an atomistic model of the underlying disorder, however, a qualitative interpretation will be provided in the following.

Three different types of diffuse scattering can be observed. The first type, narrow peaks beneath strong Bragg reflections, can be related to thermal diffuse scattering (TDS). The intensities of the diffuse peaks tend to increase with the scattering angle and with the intensity of the corresponding Bragg reflections. In general, the diffuse peaks are elongated along directions perpendicular to the scattering vector of the corresponding Bragg peaks. Beneath the strongest reflections these diffuse features show a butterfly-like shape that is frequently observed for TDS (see, *e.g.*, reflections 0 4 0 and 0 8 0 in Fig. 1a).

The second type of diffuse scattering shows some similarities with TDS. The narrow peaks are also centered at Bragg positions and the intensities tend to become stronger with increasing scattering angle indicating displacive disorder. In contrast to TDS, the shape of the features is more isotropic and the intensity of the diffuse peaks is not obviously correlated with the intensity of the corresponding Bragg peaks. In the 0 *k l* plane it is striking that the diffuse maxima are also present at extinct Bragg positions, *i.e.* at $k + l = 2n + 1$ (Fig. 1c). Obviously, this kind of diffuse scattering reflects a domain structure where the domains do not show the *n*-glide planes present in the average structure. From the full width at half maximum (FWHM) of the diffuse peaks, about 0.01 Å^{-1}, the domain size can be estimated to about 100 Å. A more detailed description of this kind of diffuse scattering is abandoned as most of such maxima coincide with the generally stronger TDS described above.

The third type is represented by diffuse layers located at half integer *k* indices. Along **b***, the layers have a FWHM of about 0.02 Å^{-1} indicative of rod-like domains of ~50 Å length along **b**. The strongest diffuse intensities are observed in the reciprocal space layers with $k = \pm 3.5$ and ± 7.5. They peak at *h*, *k* indices where the strongest Bragg reflections are found in the layer $k = 0$ (compare Fig. 1b and d). Since the layers are found at half integer *k* indices, the actual periodicity along the *b* axis is doubled to eight layers in each domain, while it is only four layers in the space-average.

The relatively strong background close to the origin of reciprocal space is most probably due to air scattering. However, contributions from spatially uncorrelated substitutional disorder (*monotonic Laue scattering*) cannot be ruled out.

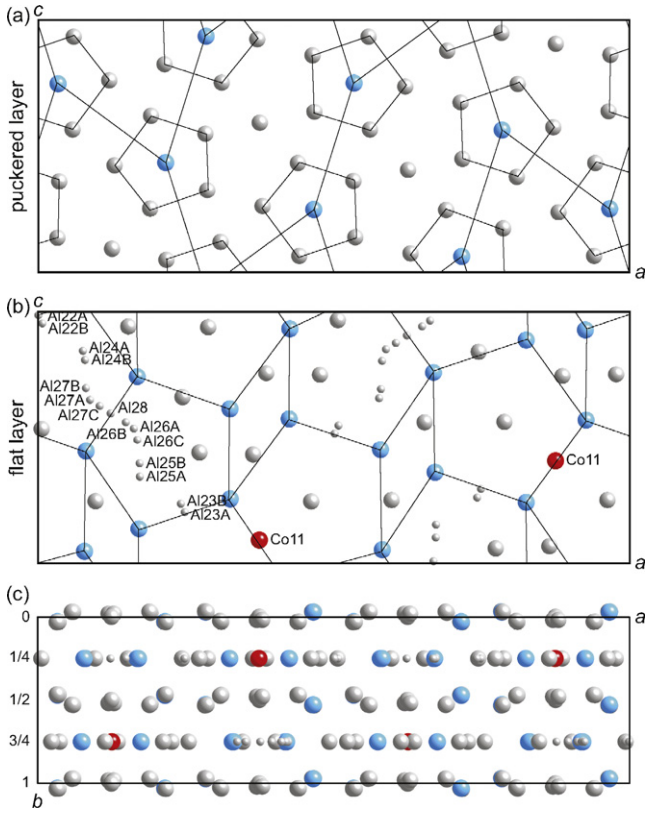

Fig. 2. Crystal structure of o'-$Al_{13}Co_4$. (0 1 0) section of one unit cell at $y = 0$ (a) and $y = 0.25$ (b) is shown. Al atoms are gray-colored, Co atoms are blue. Co atoms occupy the vertices of a hexagon tiling in (a) and of a pentagon/rhomb tiling in (b). Partially occupied Al sites are marked by small spheres. The partially occupied Co11 atom is shown in red. (c) Projection of the crystal structure along [0 0 1]. (For interpretation of the references to color in this figure legend, the reader is referred to the web version of the article.)

3.4. First-principles calculations and stability

All density functional theory calculations have been performed with the VASP (Vienna *ab initio* simulation package) [32,33] code, using the generalized gradient approximation (GGA) [34] together with the all-electron projector augmented wave [35] method to relax the structures and calculate the charge distribution at 0 K. In all calculations the projector augmented wave (PAW) potentials

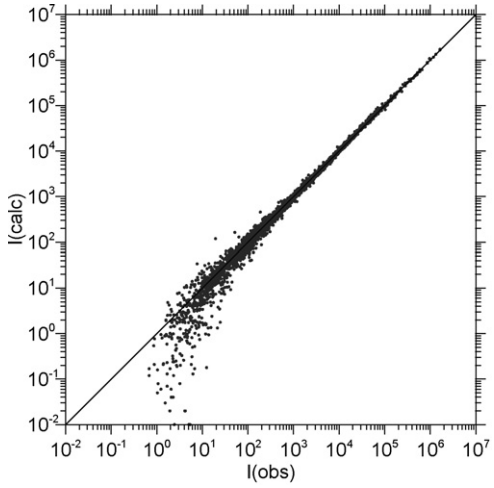

Fig. 3. Plot of I_{obs} *vs.* I_{calc} of the final model for o'-$Al_{13}Co_4$.

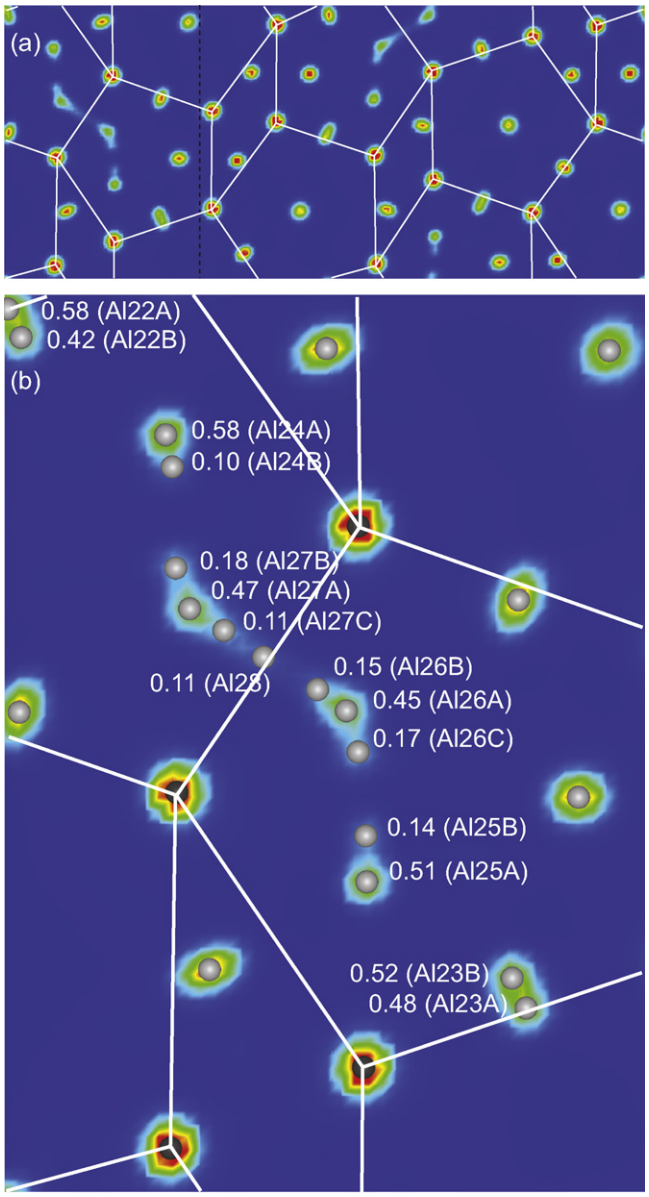

Fig. 4. (a) (0 1 0) section of the o'-$Al_{13}Co_4$ unit cell at $y = 0.25$ (flat layer) calculated by MEM. (b) Enlarged part of the calculated electron density map (left part from the black dotted line in (a)) superimposed with the refined model (Al: gray, Co: black; SOF of Al split positions are given). The white pentagon/rhomb tiling corresponds to that in Fig. 2b.

and the Monkhorst–Pack scheme [36] for the Brillouin zone sampling has been used. The plane wave kinetic energy cut-off was set to 268 eV, and the reciprocal resolution for k-points of $2\pi 0.125$ Å^{-1}. Atomic positions and lattice parameters were relaxed using the conjugate gradient algorithm. The energy minimization procedure is iterative and proceeds until self-consistency within a prescribed tolerance of 10^{-5} eV per unit cell for electronic optimization and 10^{-4} eV per unit cell for ionic relaxation. Thus we were able to achieve a target precision of 0.5 meV/atom on all relative energies.

As starting point for the calculations, the enthalpies of the stable structures (Al, Al_9Co_2, Al_5Co_2, AlCo and Co) in the Al–Co binary have been calculated. Several hypothetical structure models of o- and m-$Al_{13}Co_4$ including different vacancy distributions have been added as references and plotted using the convex hull scheme, analogously to [37]. Our convex hull shows generally the same characteristic as previous calculations [37], but is lower in the enthalpy differences. This is due to a different setting in the

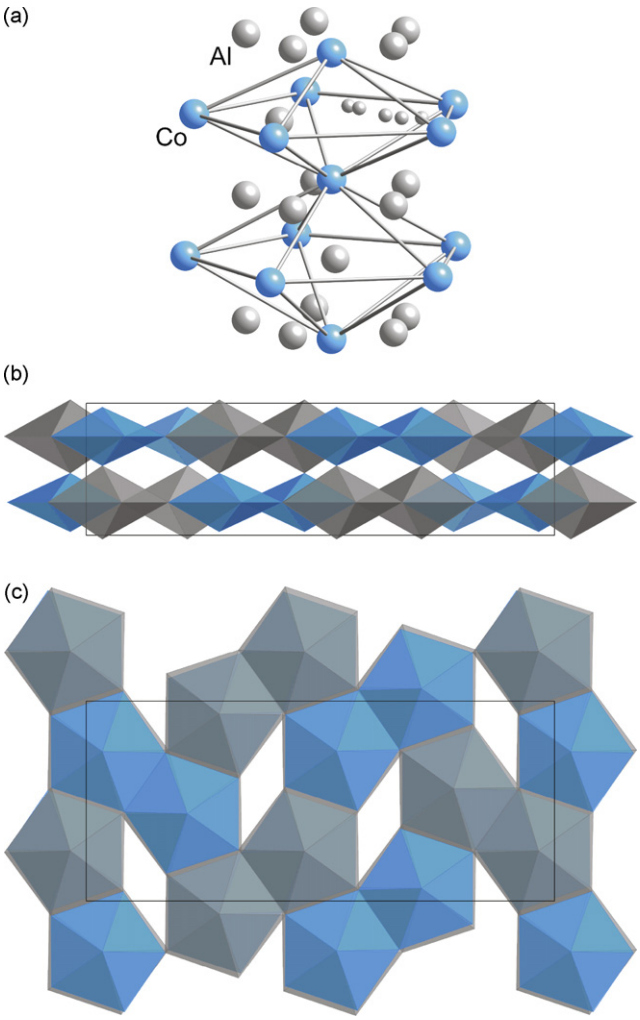

Fig. 5. (a) Structure of the pentagonal bipyramids formed by the Co atoms in o'-$Al_{13}Co_4$. (b) Flat (blue) and elongated (gray) PBPs alternate along [0 0 1]. (c) distribution of the two kinds of PBPs in the pseudo-quasiperiodic (1 0 1) planes. (For interpretation of the references to color in this figure legend, the reader is referred to the web version of the article.)

input which avoids wrap around errors and uses an augmentation grid that is exactly twice as large as the coarse grid for the representation of the pseudo-wave-functions, hence our calculations represent the enthalpy differences in the system with an increased accuracy.

In the VASP code it is not possible to use partial occupancies as input, hence the structure models need to be idealized, *i.e.* a choice must be made concerning which sites are occupied and which contain a vacancy. In the following we describe the different models used for a given structure.

To start with the first-principles calculations on the o'-$Al_{13}Co_4$ phase, the refined structure was idealized to circumvent the complexity in the Al split positions. Primary Al split-atoms with high SOF (Al22A–Al27A) were fully occupied in the initial model and minor Al split positions (labeled with B and C and Al28, *cf.* Fig. 2) were not considered. We denominate this model o'-$Al_{13}Co_4$-M1, having a composition of $Al_{156}Co_{48}$ and a total of 204 atoms. No split positions are observed in the o-$Al_{13}Co_4$ and m-$Al_{13}Co_4$ structures, thus an idealization was not necessary for the calculations. Denominated here as o-$Al_{13}Co_4$-M1 and m-$Al_{13}Co_4$-M1, with a composition of $Al_{78}Co_{24}$ and a total 102 atoms for both. In a first step, we calculated the relaxed structures at 0 K and the enthalpies for o'-$Al_{13}Co_4$-M1, o-$Al_{13}Co_4$-M1 and m-$Al_{13}Co_4$-M1 models without any vacancies.

In a next step the three phases were modeled by adding vacancies. In order to preserve the stoichiometry for all three phases, the partially occupied Co atom Co11 in the o'-$Al_{13}Co_4$ phase was set to be a fully occupied Al position. According to the refinement of o'-$Al_{13}Co_4$, one zigzag line includes one vacancy (*cf.* Section 3.1) and the split positions corresponding to Al24–Al27 are partially occupied. Accounting for the partial occupation of Al positions, the previously described idealized o'-$Al_{13}Co_4$-M1 and o-$Al_{13}Co_4$-M1 structure models were described with one vacancy per zigzag line.

Four possibilities of vacancies ordering were investigated in the o'-$Al_{13}Co_4$ and o-$Al_{13}Co_4$ phases, keeping the symmetry of related Al positions. This yielded in 4 vacancies (one per zigzag chain) for o'-$Al_{13}Co_4$, resulting in the model o'-$Al_{13}Co_4$-M2, and 2 vacancies for o-$Al_{13}Co_4$, resulting in the model o-$Al_{13}Co_4$-M2. The o-$Al_{13}Co_4$ structure was refined without partial occupation, but its stability range extends towards smaller Al-content [4,3]. For a comparison of stability with o'-$Al_{13}Co_4$ the model was made to have the same stoichiometry. The structures based on the m-$Al_{13}Co_4$ phase comprise 3 vacancies on Al sites, denominated m-$Al_{13}Co_4$-M2. Structure refinement shows one Al position with approximate occupation 0.5 and one Al position with occupation close to 0.75 and both Al positions with multiplicity 4 [27], we modeled two of four and one of four of the symmetry-related Al positions with vacancies, respectively.

Based on the refined data, the partially occupied Co atom (Co11, SOF ≈ 0.5) was taken into account, leading to a $2\times1\times1$ superstructure of the o'-$Al_{13}Co_4$ phase, denominated o'-$Al_{13}Co_4$-M3. The structure was doubled along the $\sim$8 Å direction. The final model involves 2 vacancies for the four Co11-positions and 8 vacancies for Al positions, resulting in 12 vacancies. The Al-vacancies were distributed as described above for the o'-$Al_{13}Co_4$-M2 containing four Al-vacancies.

Fig. 8 shows the enthalpy difference of all the structure models normalized to the tie-line of Al_5Co_2–Al_9Co_2, *i.e.* the reaction enthalpy of the model decomposing into Al_5Co_2 and Al_9Co_2. If

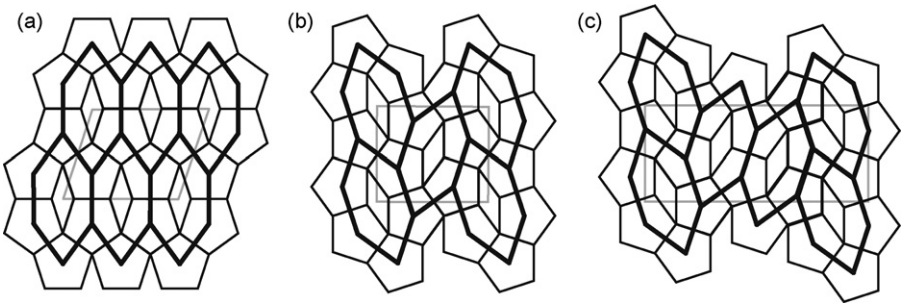

Fig. 6. Tilings characterizing the relationships between the closely related structures of (a) m-$Al_{13}Co_4$, (b) o-$Al_{13}Co_4$ and (c) o'-$Al_{13}Co_4$. The hexagon tilings apply to the flat layers, the pentagon/rhomb tilings to the puckered ones. The unit cells are marked by gray lines.

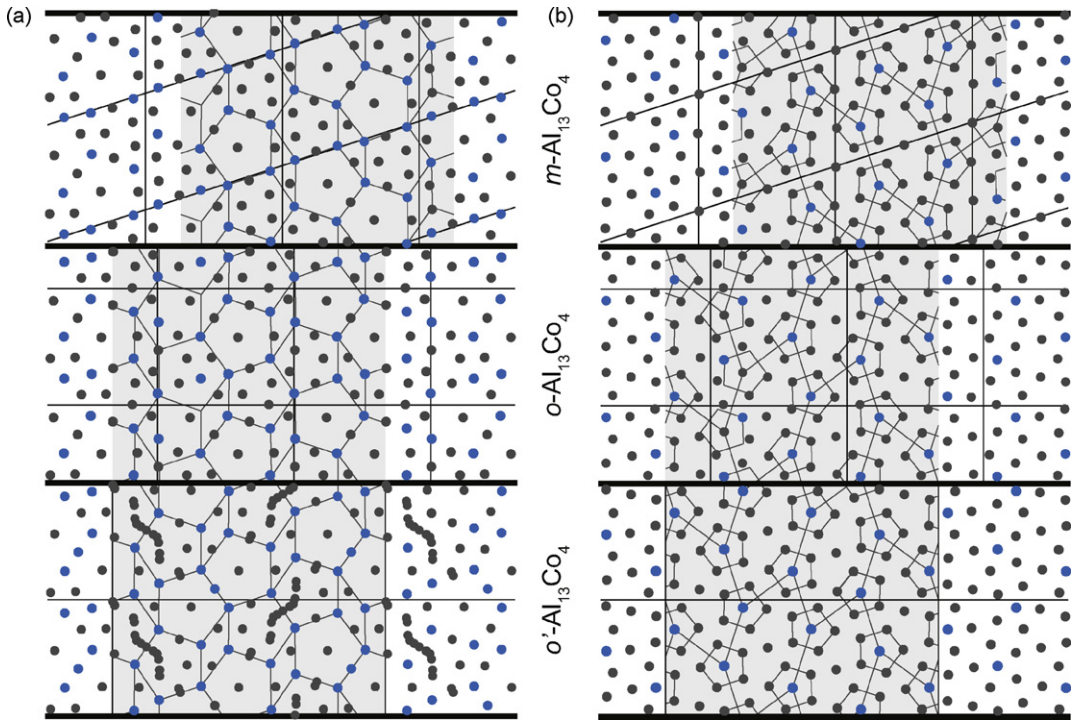

Fig. 7. Puckered (a) and flat layers (b) of m-$Al_{13}Co_4$, o-$Al_{13}Co_4$ and o'-$Al_{13}Co_4$ (Co: blue circles, Al: gray circles). The thin black lines outline the unit cells of the different structures. The shaded area marks the area of two unit cells of o'-$Al_{13}Co_4$. The rhomb/pentagon and the hexagon tiling of o'-$Al_{13}Co_4$ is overlaid to all three structures. The shaded areas mark the regions in the structures of o- and m-$Al_{13}Co_4$ where the agreement with that of o'-$Al_{13}Co_4$ is best. The origin of the zigzag sequence of Al split positions in o'-$Al_{13}Co_4$ gets clear by comparing it with the structure of m-$Al_{13}Co_4$. Note that the atoms in the puckered layers fit not only the x and y coordinates, but also the out-of-plane displacements of the atoms match in direction and amplitude. (For interpretation of the references to color in this figure legend, the reader is referred to the web version of the article.)

the enthalpy is negative, the models will be thermodynamically stable under these conditions. For a general overview the convex hull scheme over the full compositional range is shown as inset. All the investigated M1 and M2 models of o'-$Al_{13}Co_4$ and o-$Al_{13}Co_4$ are within 3 meV/atom of each other, but compared to the Al_5Co_2–Al_9Co_2 tie-line they are all slightly positive in enthalpy (Fig. 8). However, the energy of the orthorhombic structures seems to be lowered with the addition of Al-vacancies (about 2 meV/atom for o'-$Al_{13}Co_4$-M2, and up to 1.5 meV for o-$Al_{13}Co_4$-M2).

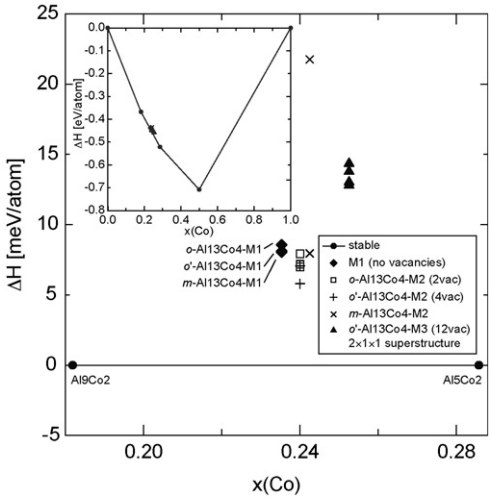

Fig. 8. Enthalpies of formation of compounds in the system Al–Co. In the inset the full compositional range is depicted, while the large figure just shows the composition range $0.18 < x_{Co} < 0.29$ normalized to the Al_5Co_2–Al_9Co_2 tie-line.

The four investigated m-$Al_{13}Co_4$-M2 structures differ significantly in energy of each other. Two have an enthalpy difference to the tie-line of more than 22 meV and can be regarded as unstable under these conditions. The other two hypothetical structures are similar in energy as the orthorhombic phases. Clearly the distribution of the vacancies is crucial to achieve a low energy model. In the structures with high energy difference the vacancies were close to each other, whereas in the low energy structure they were further apart from each other, hence influencing each other less and lowering the energy of the model.

A similar preferred vacancy distribution in o'-$Al_{13}Co_4$-M3 was not observed. All four investigated superstructures are equal in energy (within the accuracy of the method), but slightly (about 6 meV/atom) increased in energy to the other orthorhombic structure models.

In summary, all investigated hypothetical structures are above the tie-line, *i.e.* they are thermodynamically unstable towards a mixture of Al_5Co_2 and Al_9Co_2 under the given circumstances (0 K). Nevertheless the enthalpy differences between the structures and the tie-line are not big (6–9 meV/atom) and could be overcome by entropy effects such as excess vibrational and vacancy hopping entropy at high temperatures, hence the new models will be metastable or high-temperature phases. This is in agreement with the results of Mihalkovič and Widom [37] and completes them with the new phase o'-$Al_{13}Co_4$.

4. Conclusions

The new approximant o'-$Al_{13}Co_4$ was found while searching for τ^2-$Al_{13}Co_4$, the largest known approximant of decagonal Al–Co–Ni and Al–Co–Cu. From our studies, we conclude that τ^2-$Al_{13}Co_4$ may be a metastable phase that transformed into o'-$Al_{13}Co_4$ at our experimental conditions (82 d at 1050 °C).

Our first-principles calculations on hypothetical $Al_{13}Co_4$ structure models including vacancies and partial occupancies show that none of them are thermodynamically stable at 0 K. In the investigated compositional range of the phase diagram, a mixture of Al_5Co_2 and Al_9Co_2 is thermodynamically favored at low temperatures. Vacancies in the models o'-$Al_{13}Co_4$-M2 and o-$Al_{13}Co_4$-M2 lower the enthalpy difference, but still not stabilize them fully at 0 K. o'-$Al_{13}Co_4$-M2, a model with 4 vacancies, shows the lowest enthalpy indicating its role as possible high-temperature phase in the $Al_{13}TM_4$ compound family.

Acknowledgements

We thank the group of Michael Feuerbacher, Forschungszentrum Jülich for the opportunity and assistance in sample preparation, the staff of the Swiss/Norwegian beam line (SNBL) at ESRF and the beam line X06SA at the SLS and Miroslav Kobas (Dectris) for their assistance in data collection and the Swiss National Supercomputing Centre (CSCS) for access to supercomputers. Financial support by the Swiss National Foundation under grant 200020-121568 is gratefully acknowledged.

References

[1] W. Steurer, Z. Kristallogr. 219 (2004) 391–446.
[2] T. Gödecke, Z. Metallkd. 62 (1971) 842–843.
[3] B. Grushko, R. Wittenberg, K. Bickmann, C. Freiburg, J. Alloys Compd. 233 (1996) 279–287.
[4] T. Gödecke, M. Ellner, Z. Metallkd. 97 (1996) 854–864.
[5] T. Gödecke, Z. Metallkd. 88 (1997) 904–910.
[6] R.C. Hudd, W.H. Taylor, Acta Crystallogr. 15 (1962) 441–442.
[7] P.J. Black, Acta Crystallogr. 8 (1955) 43–48.
[8] P.J. Black, Acta Crystallogr. 8 (1955) 175–182.
[9] L.E. Edshammar, Acta Chem. Scand. 19 (1965) 2124–2130.
[10] T. Rajasekharan, N. Sarah, K. Schubert, Z. Metallkd. 73 (1985) 526–529.
[11] J. Grin, U. Burkhardt, M. Ellner, K. Peters, J. Alloys Compd. 206 (1994) 243–247.
[12] J. Dolinšek, M. Komelj, P. Jeglič, S. Vrtnik, D. Stanić, P. Popčević, J. Ivkov, A. Smontara, Z. Jagličć, P. Gille, Y. Grin, Phys. Rev. B 79 (2009) 184201.
[13] X.L. Ma, K.H. Kuo, Metall. Mater. Trans. A 23 (1992) 1121–1128.
[14] Z. Mo, K.H. Kuo, X.L. Ma, H. Sui, Metall. Mater. Trans. A 29 (1998) 1565–1572.
[15] K. Saito, T. Yokosawa, M. Tanaka, A.P. Tsai, J. Electron. Microsc. 48 (1999) 105–114.
[16] B. Grushko, C. Freiburg, K. Bickmann, R. Wittenberg, Z. Metallkd. 88 (1997) 379–381.
[17] C.H. Hu, X.Z. Li, J. Alloys Compd. 473 (2009) L25–L27.
[18] W. Kabsch, J. Appl. Cryst. 26 (1993) 795–800.
[19] T. Weber, S. Deloudi, M. Kobas, Y. Yokoyama, A. Inoue, W. Steurer, J. Appl. Cryst. 41 (2008) 669–674.
[20] P. Kraft, A. Bergamaschi, C. Broennimann, R. Dinapoli, E.F. Eikenberry, B. Henrich, I. Johnson, A. Mozzanica, C.M. Schlepütz, P.R. Willmott, B. Schmitt, J. Synchrotron Radiat. 16 (2009) 368–375.
[21] L. Palatinus, G. Chapuis, J. Appl. Cryst. 40 (2007) 786–790.
[22] G. Oszlányi, A. Sütő, Acta Crystallogr. A 60 (2004) 134–141.
[23] G. Oszlányi, A. Sütő, Acta Crystallogr. A 64 (2008) 123–134.
[24] M. Shiono, M.M. Woolfson, Acta Crystallogr. A 48 (1992) 451–456.
[25] L. Palatinus, A. van der Lee, J. Appl. Cryst. 41 (2008) 975–984.
[26] G.M. Sheldrick, Acta Crystallogr. A 64 (2008) 112–122.
[27] C. Freiburg, B. Grushko, R. Wittenberg, W. Reichert, Mater. Sci. Forum 228–231 (1996) 583–586.
[28] S. van Smaalen, L. Palatinus, M. Schneider, Acta Crystallogr. A 59 (2003) 459–469.
[29] Y. Grin, U. Burkhardt, M. Ellner, K. Peters, Z. Kristallogr. 209 (1994) 479–487.
[30] B. Zhang, V. Gramlich, W. Steurer, Z. Kristallogr. 210 (1995) 498–503.
[31] Y. Grin, K. Peters, U. Burkhardt, K. Gotzmann, M. Ellner, Z. Kristallogr. 213 (1998) 364–368.
[32] G. Kresse, J. Furthmüller, Comput. Mater. Sci. 6 (1996) 15–50.
[33] G. Kresse, J. Furthmüller, Phys. Rev. B 54 (1996) 11169–11186.
[34] J.P. Perdew, K. Burke, M. Ernzerhof, Phys. Rev. Lett. 77 (1996) 3865–3868.
[35] P.E. Blöchl, Phys. Rev. B 50 (1994) 17953–17979.
[36] H.J. Monkhorst, J.D. Pack, Phys. Rev. B 13 (1976) 5188–5192.
[37] M. Mihalkovič, M. Widom, Phys. Rev. B 75 (2007) 014207.